SCIENCE ADVANCES | RESEARCH ARTICLE

OPTICS

Optical tweeze-sectioning microscopy for 3D imaging and manipulation of suspended cells

Xing Li[1,2], Dan Dan[1], Siarhei Zavatski[3], Wenyu Gao[1,2], Qiang Zhang[1,2], Yuan Zhou[1], Jia Qian[1], Yanlong Yang[1], Xianghua Yu[1], Shaohui Yan[1], Xiaohao Xu[1,3]*, Olivier J. F. Martin[3]*, Baoli Yao[1,2]*

Optical manipulation and detection of biological particulates are crucial procedures in biophotonics. Optical sectioning (OS) opens the avenue to three-dimensional (3D) microscopy, but nonoptical approaches, including sample adhesion and mechanical scanning, have always been required in this technique, rendering it impossible to image suspended cells. Here, we develop optical tweeze-sectioning microscopy by coupling structured illumination microscopy (SIM) with holographic optical tweezers (HOTs). By sculpting light in HOTs, we demonstrate that the position fluctuations of suspended yeast cells can be optically squeezed to tens of nanometers, which is sufficient for the implementation of OS with SIM. Sample scanning is achieved through optical delivery of the cells, instead of translation stages as in the conventional way. Our work presents an all-optical solution for OS, broadening its application to nonadherent, suspended cells. It further furnishes the original technique that enables both SIM-based 3D imaging and optical manipulation.

INTRODUCTION

Optical sectioning (OS) enables the differentiation of the in-focus signal from the out-of-focus background, which is essential for volume microscopy of cells or thick tissues (*1*, *2*). This can be achieved using various demodulation systems, including confocal (*3*), two-photon (*4*), light sheet (*5*, *6*), and structured illumination microscopy (SIM) (*7*, *8*). However, current state-of-the-art OS techniques rely on adhesive or mechanical forces for sample fixing and scanning, which are unavailable to cells suspended in high-fluidity environments (e.g., water and air). Extending OS to these nonadherent targets is of crucial importance for bioimaging because in situ living cells may lack mechanical attachment or support. Besides, artificial adhesion may substantially disturb the physiology of cells.

Developing in parallel yet independently of OS, optical tweezers have firmly established themselves as an important instrument in modern biophotonics, initially devised for noncontact manipulation of minute objects (*9*–*11*). In particular, holographic optical tweezers (HOTs) enable the simultaneous manipulation of multiple cells using customized structured light (*12*–*14*). Although the combination of fluorescence microscopy and optical tweezers for imaging has been successfully applied over the past decade (*15*–*17*), it is still limited to two-dimensional exploration.

Here, we propose a method for the three-dimensional (3D) imaging of suspended cells by synergically integrating SIM-based OS with HOTs, which is referred to as optical tweeze-sectioning microscopy. A remarkable feature of this method is its utilization of optical forces for both cell immobilization and axial scanning, enabling the acquisition of three-step phase-shifting images at each slice, which are subsequently reconstructed into OS 3D images, as illustrated in Fig. 1. The method therefore is all-optical, eliminating the need for coated surfaces to affix the samples and circumventing the use of translation stages. Moreover, we introduce a formula to quantify the effect of residual stripes in the reconstructed images, a challenge specific to SIM-based OS (*18*, *19*). We also demonstrate that the effect from residual stripes can be minimized by preprocessing raw images with a background filter. Last, our microscopy method enables the assembly with controllable cell-cell distances and imaging of multiple desired targets, excluding undesired ones, which offers a unique platform for studying intercellular interaction and biomechanics.

RESULTS

Stability of cells trapped by structured HOTs

Our experiments are conducted using optically trapped yeast cells in suspension. Optical tweeze-sectioning microscopy relies on two structured light fields with different wavelengths: one for the SIM and the other for HOTs (see fig. S1 and Materials and Methods for details). Unlike conventional optical traps with Gaussian intensity profiles, we shape each trap in HOTs into a petal-like field with a wider lateral dimension (Fig. 2A). This structured trap is more suitable for trapping microsized cells as it generates intensity gradients on the cell boundaries, enhancing the trapping stability (*20*). Also, the highly anisotropic field can inhibit the cell rotation because of Brownian motion.

Figure 2B shows an array of 3 by 3 traps where nine yeast cells are trapped simultaneously. The optical power for each trap is set at 50 mW. Each trapped cell exhibits a bright edge because of diffraction. Because SIM requires a certain degree of sample stability, it is necessary to investigate the position fluctuation of trapped cells. We capture 2000 bright-field images and extract the centroid of each cell from them. For cell no. 5, which has a nearly round edge, the position fluctuation is restricted within a circular area, with standard deviations of 52.7 nm in the x direction and 51.1 nm in the y direction. Figure 2C shows the standard deviations of the positions of all nine cells, with all values being below 100 nm. The mean velocity of the cells upon fluctuations is about 13 μm/s (Fig. 2D).

We next vary the optical power in the trap from 10 to 100 mW to study the cell fluctuations. For example, Fig. 2E shows the fluctuation velocity of cell no. 3 at different powers. It is seen from the figure that

---

[1] State Key Laboratory of Ultrafast Optical Science and Technology, Xi'an Institute of Optics and Precision Mechanics, Chinese Academy of Sciences, Xi'an 710119, China. [2] University of Chinese Academy of Sciences, Beijing 100049, China. [3] Nanophotonics and Metrology Laboratory (NAM), Swiss Federal Institute of Technology Lausanne (EPFL), Lausanne 1015, Switzerland.
*Corresponding author. Email: xuxiaohao@opt.ac.cn (X.X.); olivier.martin@epfl.ch (O.J.F.M.); yaobl@opt.ac.cn (B.Y.)

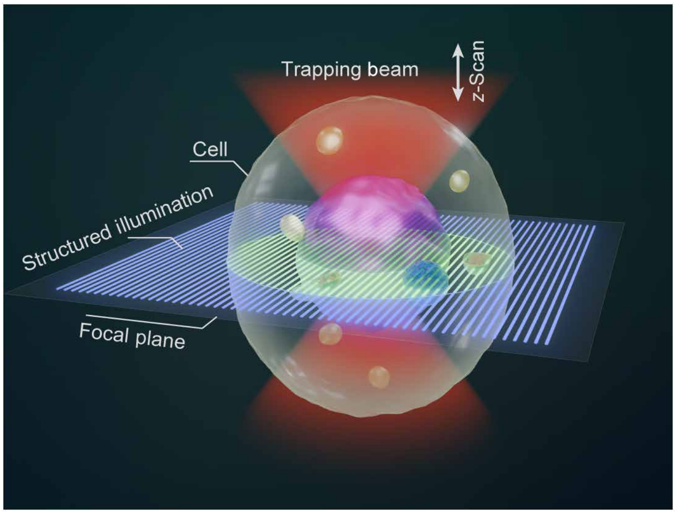

Fig. 1. Principle of optical tweeze-sectioning microscopy. Initially, cells are trapped and localized by means of HOTs. Subsequently, the trapped cells are illuminated with structured light, and three-step phase-shifting images are synchronously acquired. Last, HOTs are used to axially translate the cells, thereby obtaining *z*-stack images.

the average fluctuation velocity $\bar{v}$ decreases with increasing trapping power as $\bar{v} = \frac{a}{1+(P_{\mathrm{trap}}/b)^{c}}$, where the parameters *a*, *b*, and *c* are shown in Table 1. The standard deviations of positions for nine cells at different powers are shown in the top panel of Fig. 2F. The mean standard deviations ($\bar{\sigma}_x$ and $\bar{\sigma}_y$) decrease with increasing power P_{trap}, which are fitted by the equipartition theorem: $\bar{\sigma}_i \propto 1/\sqrt{P_{\mathrm{trap}}}$ (see the bottom panel in Fig. 2F and Table 1). When $P_{\mathrm{trap}} = 50$ mW, by means of these fitting formulas, the mean velocity of the cell in the trap is $\bar{v} = 13.42$ μm/s and the mean standard deviations are $\bar{\sigma}_x = 52.74$ nm and $\bar{\sigma}_y = 45.03$ nm. Furthermore, we extract from videos the cells' orientational fluctuations in the lateral plane (see fig. S2 for details). It shows a mean standard deviation of $\bar{\sigma}_\alpha = 0.54°$ for the nine yeasts at $P_{\mathrm{trap}} = 50$ mW; a higher power yields smaller $\bar{\sigma}_\alpha$. We can thus infer that angular trapping occurred and a stable cell orientation was maintained during the entire experiment. In principle, the angular trapping is caused by torsional optical torques (*21*), which arise when both the particle and field are not axially symmetrical. In our configuration, the asymmetry is attributed to the petal-like optical traps (Fig. 2A) and the fact that the cells have a cross section with a nonperfect circular shape (Fig. 2B).

We note that the cell should also undergo Brownian motion in the axial direction, which cannot be detected by the camera. The axial fluctuation is thus analyzed by combining the Langevin equation and optical force theory, which shows an axial standard deviation twice those in the transverse directions (see fig. S3 for details). The larger deviation in the axial direction is as expected because of the weaker axial trapping force (fig. S3B). A common way to enhance the robustness of axial trapping is the use of a counterpropagating configuration, which can create a sharp intensity gradient along the axial direction (*22*).

The suppressed position fluctuations (a few tens to a few hundreds of nanometers) offer a prerequisite for the implementation of SIM-based OS on suspended cells. The resolution of the imaging optical path can be obtained by simulating the point spread function. Theoretically, the lateral and axial resolutions are about 230 and 1100 nm, respectively, when using an oil-immersed objective and taking into account refractive index changes. In the case of a water-immersed objective, they are 207 and 560 nm, respectively. Because the Brownian fluctuations are smaller than the resolutions, they have little effect on the precision of OS by SIM.

Axial optical translation of cells for SIM-based OS

Owing to the 3D manipulation capabilities of HOTs, the suspended yeast cells can be optically translated along the *z* axis. This translation is achieved by sequentially addressing computer-generated holograms (CGHs) to the spatial light modulator (SLM), with each axial position z_n ($n = 1, \ldots, N$) corresponding to a CGH (Fig. 3A). At the same time, the trapped cells are illuminated by the stripe-structured light with a period of 452.5 nm, which undergoes three-step phase shifts (0, 2π/3, 4π/3) (Fig. 3B). Consequently, the camera captures three raw images (Fig. 3C). The timing diagram of key steps is shown in Fig. 3D, where T_1, T_2, and T_3 are 100, 0.6, and 100 ms, respectively (Fig. 3G, left).

After acquiring the raw images, the OS images are reconstructed in two steps (Fig. 3E). Step 1 involves enhancing the modulation depth via background filtering, which can be achieved by either the physical model–based method (*23*) or the rolling ball method in Fiji (*24*), with the latter being slightly less effective. Step 2 includes image reconstruction based on the root mean square (RMS) algorithm, which is the fastest and easiest way to obtain an OS image (*18*). The times consumed for the two steps are 48.5 and 1.4 ms, respectively, averaged over 100 runs on a central processing unit (Intel Xeon E5-1620 version 3) (Fig. 3G, right).

To emphasize the significance of modulation enhancement in reconstruction, we compare the OS images with and without step 1 (Fig. 3F). The OS image without step 1 displays substantial residual stripes, which are nearly eliminated when step 1 is applied. To quantify this, we introduce the concept of residual stripe contrast C_{rs} (see Eq. 2). By calculating C_{rs} for 70 OS images, we obtain an average C_{rs} of 0.068 without step 1, which is considerably higher than 0.020 with step 1. The results indicate that increasing the modulation degree of structured light fringes before RMS reconstruction can effectively suppress the residual stripes in OS images.

It is important to note that the fluctuations of the cell position do not cause the residual stripes. In the case of yeast cells adsorbed onto a coverslip, similar residual stripes are observed for the RMS reconstruction performed without step 1. In addition, the structured illumination has a stripe period of 452.5 nm, much larger than the standard deviation (tens of nanometers) of position fluctuations. Residual stripes primarily arise from changes in the defocused background during the phase-shifting process and are less influenced by phase-shift errors and fringe frequency errors. One may decrease the relative intensity of the out-of-focus background, thus minimizing the appearance of residual stripes by improving the modulation depth of fringes.

OS 3D imaging of suspended cell arrays and patterns

The procedure outlined above enables OS 3D imaging of suspended cell arrays using an optical power of 50 mW per trap. As shown in Fig. 4A, which is composed of maximum intensity projections (MIPs), OS provides a weaker background compared to wide-field (WF) imaging. Consequently, the in-focus information can be displayed with high contrast. To compare the differences in single slices

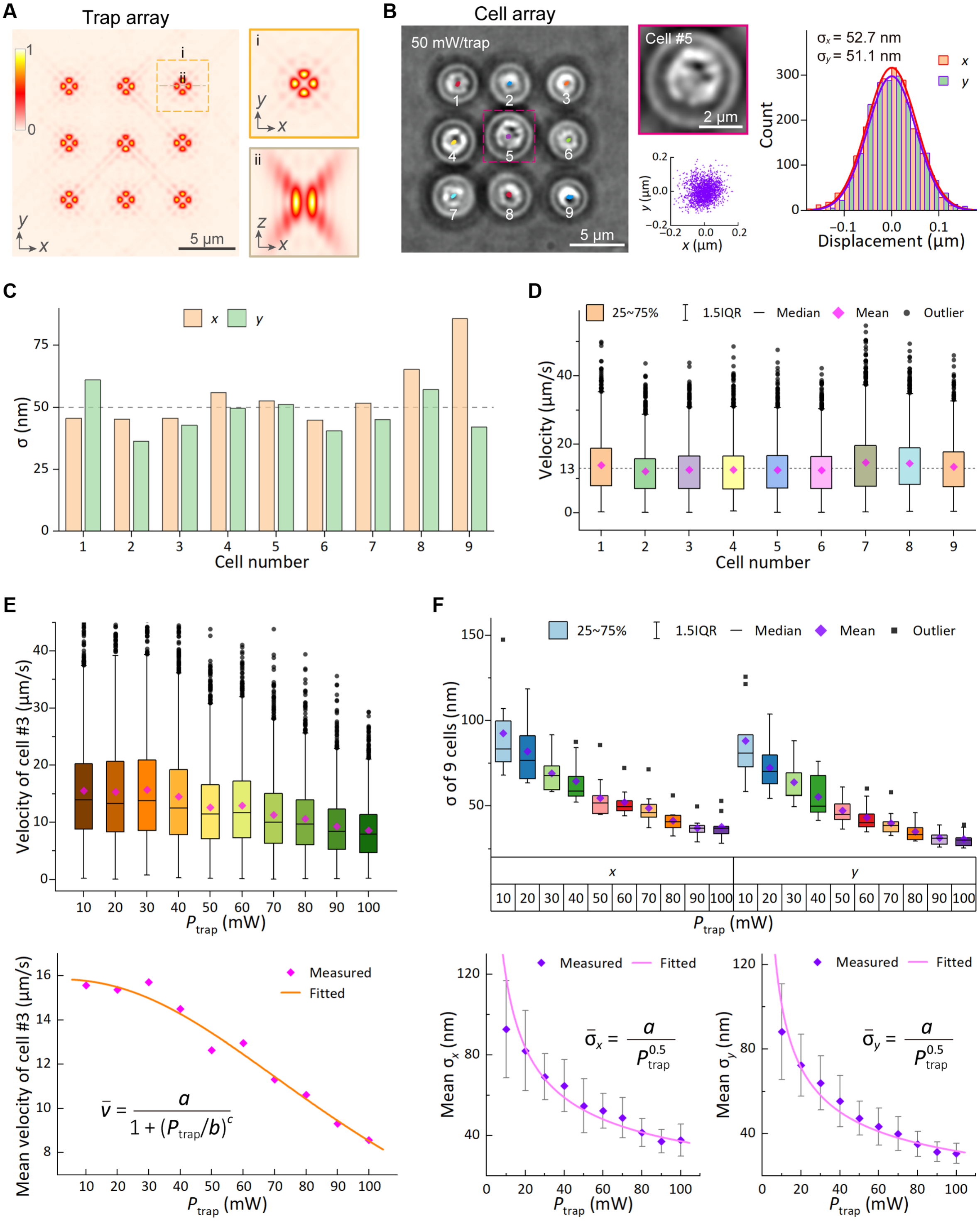

Fig. 2. Position fluctuations of yeast cells at different trap powers. (**A**) Intensity distributions of a petal-like trap array. The transverse (i) and axial (ii) views show the intensity profiles of the optical trap in the upper-right corner of the array. (**B**) Nine yeast cells immobilized by the trap array in (A). The optical power for each cell is 50 mW. The standard deviations of position fluctuations for cell no.5 are 52.7 and 51.1 nm in the *x* and *y* directions, respectively. The position data of the cells are extracted from 2000 bright-field images. (**C** and **D**) Standard deviations of positions and fluctuation speed distributions for the nine cells. (**E**) Distributions of fluctuation speeds for cell no. 3 in (B) at different trap powers (top) and the result of fitting the mean speed to the trap power (bottom). (**F**) Standard deviation distributions of positions for all nine cells in (B) at different trap powers (top) and results of fitting the mean standard deviation to the trap power (bottom).

Table 1. Fitting results for cell fluctuations. R^2 is the correlation coefficient.

Fitting function	*a*	*b*	*c*	R^2
$\overline{v} = \frac{a}{1+(P_{\text{trap}}/b)^c}$	15.85480	107.12841	2.24075	0.97466
$\overline{\sigma}_x = \frac{a}{P_{\text{trap}}^{0.5}}$	372.91055	–	–	0.89487
$\overline{\sigma}_y = \frac{a}{P_{\text{trap}}^{0.5}}$	318.41018	–	–	0.94823

between WF and OS images, the imaging results are presented in the form of *z* sections within movie S1. Because the lateral resolution of an optical microscope is higher than the axial resolution, transverse views (Fig. 4B) reveal more cellular details compared to longitudinal ones (Fig. 4C). Furthermore, a larger array of 4 by 4 cells can be created by trapping more cells (Fig. 4D). The middle image in Fig. 4D shows the out-of-focus background removed from the WF. The line plots in Fig. 4 (E and F) indicate that the out-of-focus background is notably stronger than the OS image. In addition, the axial view reveals that the yeast cells resemble rugby balls and tend to align their long axes with the optical axis. The 3D renderings of OS imaging results for the 3 by 3 and 4 by 4 cell patterns are shown in movies S2 and S3, respectively.

With optical tweeze-sectioning microscopy, one may also arrange cells into customized patterns and then perform the 3D imaging with OS. The cells can be assembled into circular, hexagonal geometries (Fig. 5). Figure 5A shows a circular arrangement of 12 yeast cells, while Fig. 5 (B and C) depicts sectional views of the cell located in the lower right corner of Fig. 5A. Each yeast cell features a dark shell surrounding a bright core. The average diameters of the shells are measured to be 4.16 μm in the transverse direction and 6.21 μm in the axial direction. Meanwhile, for the cores, the corresponding values are 2.72 and 4.34 μm, respectively (Fig. 5D). The mean ellipticity of shells is 0.67, and that of cores is 0.63 (Fig. 5E). Figure 5F depicts a hexagonal pattern formed by 12 yeast cells. The 3D views visualize the spatial positions of all cells (Fig. 5G). The 3D renderings of OS imaging results for the circular and hexagonal geometries are shown in movies S4 and S5, respectively. In addition, we explored the assembly and imaging of other geometric patterns such as pentagons, quadrilaterals, and triangles (see fig. S4 for details).

DISCUSSION

We have developed optical tweeze-sectioning microscopy for 3D imaging of suspended cells. HOTs play a crucial role in the proposed method, facilitating the microscopy in three key aspects. First, it suppresses the Brownian motion of the suspended cells so that their positional fluctuations can be smaller than the imaging resolution and the stripe period of structured illumination, which is essential for SIM. Second, HOTs enable the axial scanning of suspended cells required for OS 3D imaging. This may replace the need for translation stages, thereby reducing potential mechanical vibrations and minimizing perturbations to the samples. Last, equipped with HOTs, the microscopy has evolved into a versatile biophotonic technique, featuring not only 3D imaging capabilities but also 3D parallel manipulation functions, including trapping, delivery, and rotation.

Our method provides the scanning speed given by $s \times f_{\text{slm}}$, where s is the step size and f_{slm} is the refresh frequency of the phase-only liquid crystal SLM. During our experiments, we maintained a step size s of 0.1614 μm and a refresh frequency f_{slm} of ~10 Hz, resulting in an effective scanning speed of about 1.6 μm/s. At this level, cells remain stable within the optical traps and do not undergo noticeable wobbling. While higher scanning speeds can be achieved by increasing either s or f_{slm}, this may reduce the stability of cell manipulation. In that respect, it will be interesting to study the temporal dynamics of the cells during *z* scanning, which, however, cannot be precisely analyzed by the video tracking method. To reach this goal, one may use the power spectral method (*25*), as it tracks target's dynamics by the scattering signals of trapping light, which are collected by additional photodetectors (independent of imaging).

The risk of photodamage is a matter of concern for cell manipulation. In our study, we took several precautions to mitigate this risk. On the one hand, we have used for the optical traps a biocompatible near-infrared wavelength (1064 nm), which is generally considered a noninvasive wavelength that minimizes the extent of light-induced cell damage (*26*). Moreover, we have used petal-like traps with a wider lateral dimension instead of standard Gaussian traps, which effectively reduced the power density experienced by the cells. As a matter of fact, we did not observe damage to the cells (e.g., decomposition or deformation) in the experiment, even at the highest power (100 mW).

Let us also note that the proposed method has been currently tested only on yeast cells. Nevertheless, we trust that it is applicable for 3D trapping and imaging of most microscale cell populations (e.g., lymphocytes and tumor cells). For smaller cells (e.g., *Escherichia coli*), stable trapping could be challenging because of weaker optical forces. Further increasing the laser power can strengthen the forces, but it may cause potential photodamage to the cells. A promising way to address this issue would be doping the cells with lanthanide ions, which has been shown to greatly increase the trapping stiffness for nanoparticles (*27*). For the trapping of softer or easily deformable cells, the petal-like traps might not suffice to overcome the deformation because of Brownian motion; hence, multipoint traps should be designed. In this regard, HOTs had demonstrated an excellent ability to customize optical force fields (*12*–*14*).

Besides, the cells in this study are positioned in the transverse plane, which means that the range of axial movement is roughly equivalent to the long axis of the cell. By strategically designing the positions of optical traps, it is also possible to construct a 3D pattern of cells. However, at large depths, the trapping force is weakened by pronounced aberration. Using a water-immersed objective lens instead of an oil-immersed one can help resolve this issue. At last, despite the reported experiments in water, our adhesion-free microscopy should also be applicable in gaseous environments (*28*) and levitated optomechanical systems (*22*, *29*).

Last, it should be noted that while OS allows for imaging the 3D core-shell morphology of the yeast cells, its resolution remains constrained by the optical diffraction limit and hence is unable to image

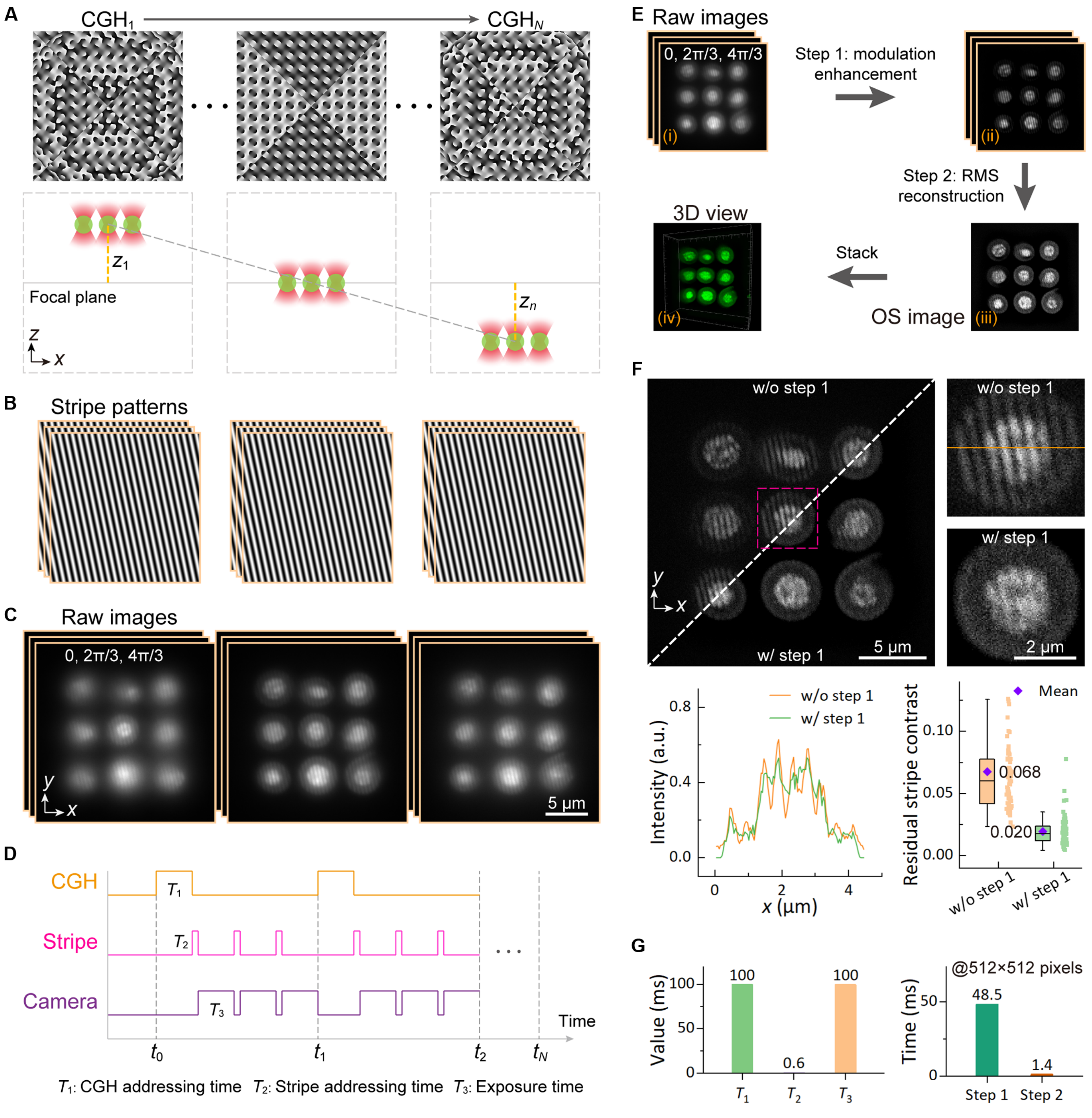

Fig. 3. Simultaneous axial translation manipulation and stripe-structured illumination for cell arrays. (**A**) CGHs addressed to a phase-only liquid crystal SLM and the linear movement of an array assembled from trapped cells along the *z* axis. (**B**) Stripes addressed to a ferroelectric liquid crystal SLM for generating structured light at each axial position. (**C**) Three-step phase-shifting raw images acquired synchronously. (**D**) Timing diagram of the CGHs, stripes, and the camera. (**E**) Procedure for reconstructing OS images starting from raw images. (i) Three raw images acquired at each axial position z_n ($n = 1, ..., N$). (ii) For each raw image, the modulation depth is enhanced using a background filter. (iii) OS image reconstructed using the RMS algorithm. Every three images produce an OS image. (iv) Pseudo-color 3D rendering of OS images for all axial positions (all z_n). (**F**) The step of modulation enhancement can substantially reduce residual stripes. a.u., arbitrary units. (**G**) Time for each hardware in the experiment and time for each step in the image reconstruction.

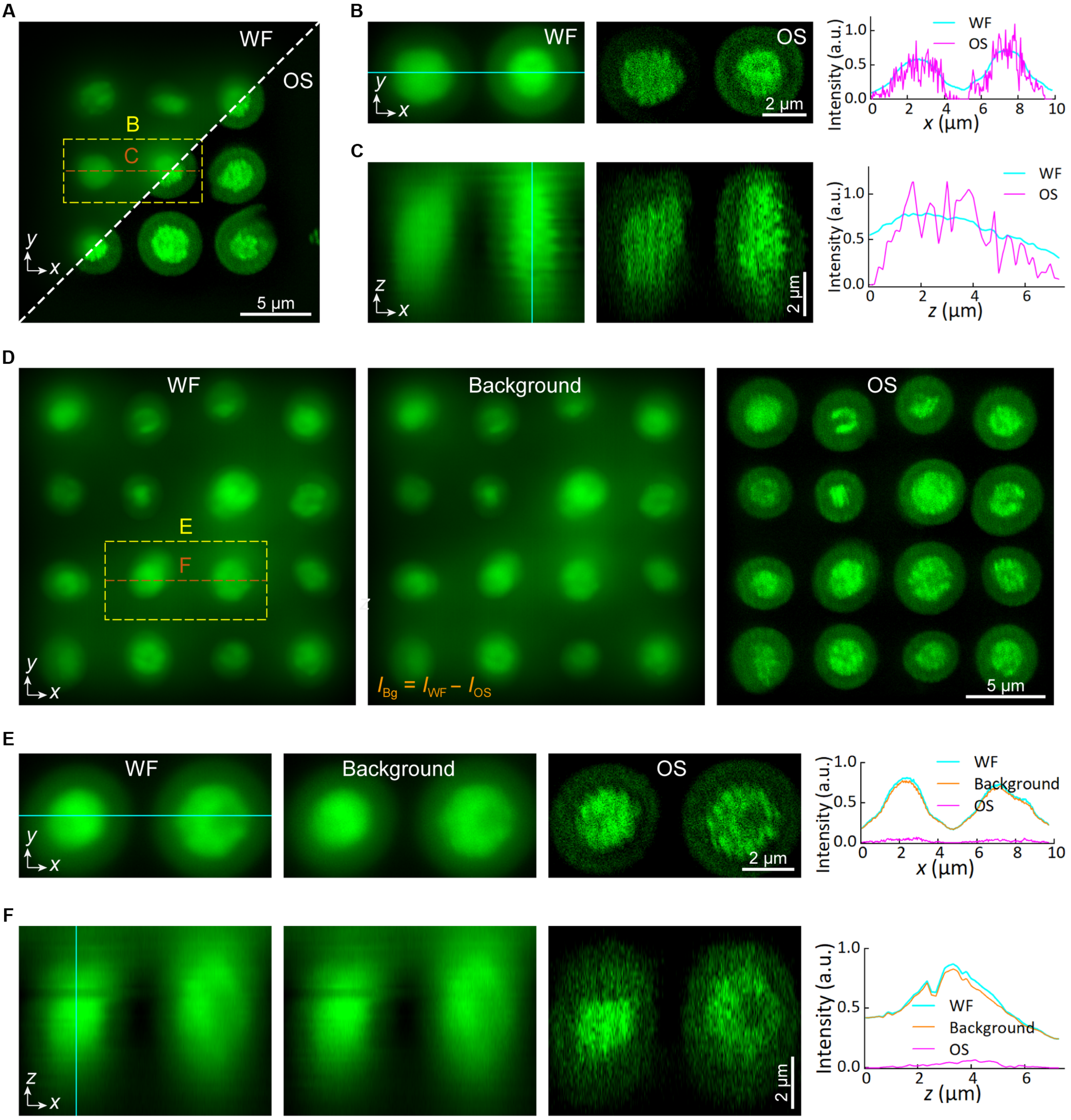

Fig. 4. OS 3D imaging of yeast cell arrays. (**A**) Maximum intensity projections (MIPs) of WF and OS images of a 3 by 3 cell array. (**B**) Lateral views (single plane) along the yellow dashed box in (A). The right panel shows intensity profiles along the *x* axis. (**C**) Axial views (single plane) along the orange dashed line in (A). The right panel shows intensity profiles along the *z* axis. (**D**) MIPs of a 4 by 4 cell array for WF, background, and OS. The background intensity (I_{Bg}) is equal to the wide-field image intensity (I_{WF}) minus the OS intensity (I_{OS}). (**E**) Enlarged views (single plane) along the yellow dashed box in (D). Intensity profiles in the right panel are normalized by WF. (**F**) Zoomed-in views (single plane) along the orange dashed line in (D).

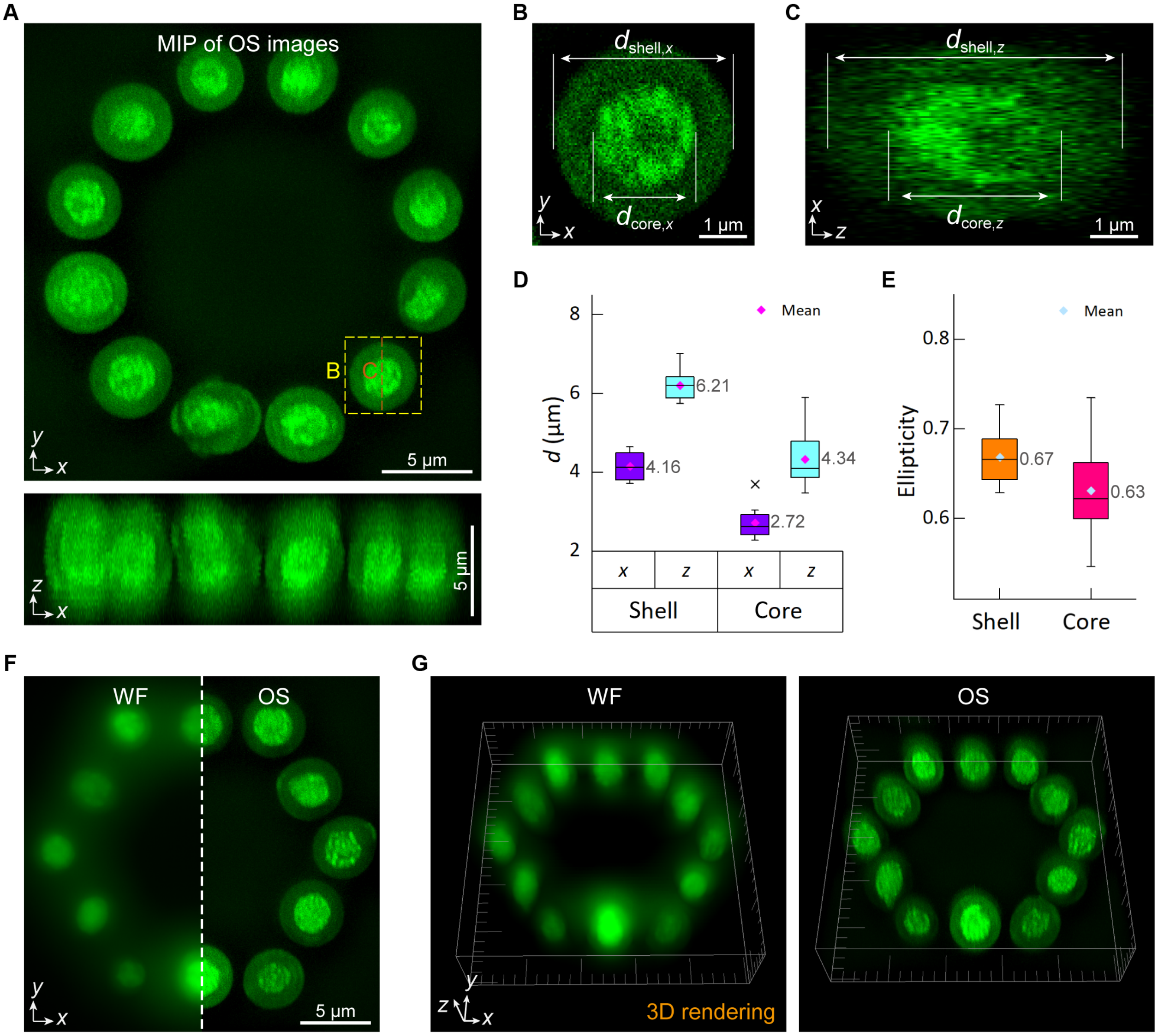

Fig. 5. OS 3D imaging of geometric patterns formed by yeast cells. (**A**) MIPs derived from OS images of a ring-like pattern consisting of 12 cells. (**B**) *x*-*y* view (single plane) along the yellow dashed box in (A). (**C**) *x*-*z* view (single plane) along the orange dashed line in (A). (**D**) Diameters of shells and cores for 12 cells. (**E**) Ellipticities of shells and cores for all cells. (**F**) MIPs of a hexagonal cell pattern. (**G**) 3D views of the hexagonal pattern.

subcellular details (e.g., mitochondria or vesicles). Going beyond this limit requires staining of specific cells to label their interior features; such super-resolution imaging can be implemented with SIM (*30*–*32*).

In summary, our work represents the initial step toward deploying 3D microscopy powered by optical tweezers, creating opportunities for OS to visualize nonadherent targets. These results may inspire the integration of optical tweezers with other microscopy techniques for applications that require high speed (*33*), isotropic resolution (*34*, *35*), large fields of view, and super-resolution imaging (*17*).

MATERIALS AND METHODS

Experimental setup

A schematic of the experimental setup combining HOTs and SIM-based OS is shown in fig. S1. In the SIM path, a 473-nm laser beam (gem 473, Laser Quantum Ltd., UK) was expanded and collimated by a telescope (L1 and L2) and was horizontally linearly polarized after passing through a half-wave plate (HWP1) and a polarizing beam splitter (PBS1). Multiple diffraction orders were generated by addressing binary stripe maps to a ferroelectric liquid crystal SLM (SLM1; 2048 by 1536 pixels, 8.2-μm pixel pitch, QXGA-3DM, Forth Dimension Displays, UK). The fast axis of HWP2 was rotated to maximize the intensities of the ±1st order beams. HPW3 converted vertically linearly polarized beams reflected by PBS1 to the s-polarized ones. The spatial filter blocked the beams of all orders except ±1st orders. The ±1st order beams were then relayed by lenses L3 and L4 to the back focal plane of an objective lens (Apo TIRF, 60×/1.49, Oil Immersion or Plan Apo IR, 60×/1.27, Water Immersion, Nikon Corp., Japan) with a high numerical aperture (NA) and interfered in the front focal plane of the objective to create fringes with a cosine intensity distribution. In the HOT path, the 1064-nm beam from the laser (VFLS-1064-B-SF-HP, Connet Laser

Technology Co., Ltd., China) was expanded and collimated by the telescope (L6 and L7) and was horizontally linearly polarized after passing through HWP4 and PBS2. A prism was used to reflect the beam so as to shorten the optical path. The incident beam was shaped by addressing a CGH to a phase-only liquid crystal SLM2 (1920 by 1080 pixels, 8-μm pixel pitch, PLUTO-2-NIR-049, Holoeye Photonics AG, Germany). The panel of SLM2 was relayed through a 4-*f* system (L8 and L9, 1:1 conjugate ratio) to the back aperture of the objective lens, and optical traps were generated in the front focal plane of the objective. A quarter-wave plate (QWP1) converted the linearly polarized beam to a circularly polarized one. Dichroic mirrors DM1 (Di03-R488/561-t1-25×36, Semrock Inc., US) and DM2 (Di02-R1064-25×36, Semrock Inc., US) enabled wavelength-specific beam combination/separation. The setup supported fluorescence imaging using a 473-nm laser or bright-field imaging using a light-emitting diode source (MCWHL7, Thorlabs Inc., US). Emission signals were separated through a filter cascade (F1: excitation; F2: emission; F3: 1064-nm notch) before detection by a scientific complementary metal-oxide semiconductor camera (2048 by 2048 pixels, 6.5-μm pixel pitch, ORCA-Flash 4.0 V2 C11440-22CU, Hamamatsu Photonics K. K., Japan). An optimized imaging path incorporating a 300-mm achromatic tube lens and a 1.8× magnification lens provided about 160× total system magnification. CGHs and SIM patterns were computationally generated using MATLAB. Hardware synchronization and image acquisition were managed through a custom software suite developed in the QT framework (version 6.5.1). The crucial experimental parameters are presented in table S1.

Image acquisition

At the onset of experiments, the pixel size was calibrated using a microscopic scale to facilitate subsequent image reconstruction. When imaging biological samples, a 473-nm laser was used to excite dyes and the fluorescence emission was collected within the wavelength range of 500 to 550 nm. Samples were axially scanned by refreshing CGHs on the SLM2 to obtain stack data. The axial step was preset to 0.15 μm in the CGHs, while the experimentally measured scanning step was 0.1614 μm. At each axial position, the samples were illuminated by stripe-structured light featuring three phase shifts (0, 2π/3, and 4π/3). Three images were synchronously acquired, with an exposure time of 100 ms for each frame.

OS image reconstruction

Cells suspended in water were trapped using an oil-immersed objective lens with a nominal NA of 1.49 and an effective NA of 1.3. The fluorescence wavelength is defined as $\lambda = 525$ nm. Consequently, the diffraction limit is calculated as $\delta = 0.5\lambda/\mathrm{NA}$, which amounts to 201.9 nm. The experimentally measured period of the stripes in the structured illumination was 452.5 nm. Therefore, the stripe frequency was ~0.45 times the cutoff frequency. When using a water-immersion objective with an effective NA of 1.27, the result was 0.46 times. Image reconstruction was accomplished in two steps. Initially, the raw images underwent preprocessing with a background filter to enhance the modulation depth of the stripe-structured illumination. Subsequently, OS reconstruction was carried out using the RMS algorithm (*18*)

$$D_{\mathrm{in}}(x,y) = \frac{\sqrt{2}}{3m}\sqrt{\left[D_1(x,y)-D_2(x,y)\right]^2+\left[D_2(x,y)-D_3(x,y)\right]^2+\left[D_3(x,y)-D_1(x,y)\right]^2} \tag{1}$$

Here, $D_1(x, y)$, $D_2(x, y)$, and $D_3(x, y)$ are images with phase shifts of 0, 2π/3, and 4π/3, respectively. m denotes the modulation depth, and $D_{\mathrm{in}}(x, y)$ represents the OS image. Note that the RMS algorithm is the algorithm of choice for OS reconstruction.

Residual stripe contrast

The reconstructed OS image may exhibit residual stripes. The intensity of these stripes can be quantitatively determined by the residual stripe contrast C_{rs}, as defined below

$$C_{\mathrm{rs}} = \frac{2\,|\tilde{D}_{\mathrm{in}}(u_{+1}, v_{+1})|}{|\tilde{D}_{\mathrm{in}}(0,0)|} \tag{2}$$

where

$$\tilde{D}_{\mathrm{in}}(u,v) = \mathrm{FFT}\left\{D_{\mathrm{in}}(x,y)\right\} \tag{3}$$

and (u_{+1}, v_{+1}) represent the center coordinates of the +1st order component within the spectrum.

Generation of optical traps

The weighted Gerchberg-Saxton algorithm (*36*) was used to generate petal-like trap arrays. To begin with, a dimensionless metric

$$V_m = \frac{1}{N}\sum_{j=1}^{N} e^{i\left(\phi_j - \Delta_j^m\right)} \tag{4}$$

where

$$\Delta_j^m = \frac{\pi z_m}{\lambda f^2}\left(x_j^2 + y_j^2\right) + \frac{2\pi}{\lambda f}\left(x_j x_m + y_j y_m\right) \tag{5}$$

is defined. ϕ_j is the phase of the jth pixel of an SLM, and N is the total number of pixels. (x_j, y_j) are the Cartesian coordinates of the jth pixel on the SLM plane, and (x_m, y_m, z_m) are the Cartesian coordinates of the mth trap. λ is the wavelength, and f is the focal length of a Fourier lens.

Subsequently, commencing with a random initial estimate for ϕ_j and assigning the weights $w_m = 1$, the iterations of the weighted Gerchberg-Saxton algorithm are carried out in the following manner

$$\begin{aligned} &\text{0th step} \qquad w_m^0 = 1, \quad \phi_j^0 = \arg\left[\sum_m e^{i\left(\Delta_j^m + \gamma_m\right)}\right] \\ &k\text{th step} \quad w_m^k = w_m^{k-1}\frac{\langle|V_m^{k-1}|\rangle_m}{|V_m^{k-1}|}, \quad \phi_j^k = \arg\left[\sum_m e^{i\Delta_j^m}\frac{w_m^k V_m^{k-1}}{|V_m^{k-1}|}\right] \end{aligned} \tag{6}$$

where γ_m is a random phase. Upon completing 30 (or more) iterations, it outputs the phase ϕ_j, which can generate Gaussian optical traps.

In the end, to get petal-like traps, the binary phases of 0 and π are superimposed onto ϕ_j

$$\psi(r,\theta) = \begin{cases} \phi_j & \text{if} \quad -\frac{\pi}{4} \le \theta < \frac{\pi}{4} \ \text{or} \ \frac{3\pi}{4} \le \theta < \frac{5\pi}{4} \\ \phi_j + \pi & \text{if} \quad \frac{\pi}{4} \le \theta < \frac{3\pi}{4} \ \text{or} \ \frac{5\pi}{4} \le \theta < \frac{7\pi}{4} \end{cases} \tag{7}$$

Here, (r, θ) denote the polar coordinates of the SLM plane. This is accomplished by saving $\psi(r, \theta)$ as a CGH.

Calibration of the scanning step

Before visualizing a 3D image, the spacing between axially adjacent layers was calibrated. Axial scanning of an optical trap was executed by incorporating the phase function exp(i$k_z z$) to the CGH. First, values z_1, z_2, ..., z_j were assigned to generate axial multifoci. Second, a piezoelectric displacement stage was used to conduct a scan along the z axis to obtain the axial intensity distribution. Last, the actual axial positions d_j corresponding to z_j were measured, and a linear fit was performed between them using the function $d = bz + a$. In fig. S5A, seven foci were designed to have an axial spacing of 1 μm. The fitting result yielded the equation $d = 1.08214z + 0.09234$, with a correlation coefficient $R^2 = 0.99928$ (as depicted in fig. S5B). In addition, the spacing was adjusted to 1.5 μm, and the corresponding seven foci were obtained, as shown in fig. S5C. The resulting fitting equation was $d = 1.06964z + 0.00577$, with a correlation coefficient $R^2 = 0.99922$ (fig. S5D). In both instances, the linear correlation coefficient R^2 between d and z approaches 1. This shows that the way the optical tweezers move the cells is linear within a certain range along the optical axis. In our experimental setup, the predefined moving step in the CGHs was $\delta_z = 0.15$ μm. Consequently, the resultant scanning step was calculated as $d_z = (b_1 + b_2)/2 \times \delta_z = 0.1614$ μm. This calibration value was measured when a 60× oil-immersed objective lens was used. The value for a 60× water-immersed objective is close to it.

Sample preparation

The yeast cell sample used in the experiments was sourced from a commercial product (Zymosan A Bioparticles, Alexa Fluor 488 conjugate, Thermo Fisher Scientific Inc., US) and had undergone staining. Initially, a limited amount of freeze-dried yeast powder was dissolved in deionized water, and then a 5-min ultrasonication process was performed to formulate a cell suspension. Subsequently, a sample chamber was constructed using a slide, a coverslip, and double-sided tape, with the chamber having a depth of ~100 μm along the z axis. Next, around 50 μl of the cell suspension was carefully aspirated and injected into the chamber, which was then sealed with an appropriate adhesive. Ultimately, the sample was examined using the custom-built experimental setup.

Statistics and reproducibility

Cell fluctuation data corresponding to each power level were extracted from a set of 2000 bright-field images by using the TrackMate plugin (version 7.13.2) (*37*) within the Fiji software (version 2.16.0). Experimental images were subjected to processing using MATLAB (release R2021a). Curve plots, bar plots, and box plots were generated using Origin (version 2018).

Supplementary Materials

The PDF file includes:
Figs. S1 to S5
Table S1
Legends for movies S1 to S5

Other Supplementary Material for this manuscript includes the following:
Movies S1 to S5

REFERENCES AND NOTES

1. J. Zhang, W. Qiao, R. Jin, H. Li, H. Gong, S.-C. Chen, Q. Luo, J. Yuan, Optical sectioning methods in three-dimensional bioimaging. *Light Sci. Appl.* **14**, 11 (2025).
2. J. Mertz, Optical sectioning microscopy with planar or structured illumination. *Nat. Methods* **8**, 811–819 (2011).
3. J.-A. Conchello, J. W. Lichtman, Optical sectioning microscopy. *Nat. Methods* **2**, 920–931 (2005).
4. W. Denk, J. H. Strickler, W. W. Webb, Two-photon laser scanning fluorescence microscopy. *Science* **248**, 73–76 (1990).
5. E. H. K. Stelzer, F. Strobl, B.-J. Chang, F. Preusser, S. Preibisch, K. McDole, R. Fiolka, Light sheet fluorescence microscopy. *Nat. Rev. Methods Primers* **1**, 73 (2021).
6. P. J. Keller, A. D. Schmidt, J. Wittbrodt, E. H. K. Stelzer, Reconstruction of zebrafish early embryonic development by scanned light sheet microscopy. *Science* **322**, 1065–1069 (2008).
7. Z. Li, Q. Zhang, S.-W. Chou, Z. Newman, R. Turcotte, R. Natan, Q. Dai, E. Y. Isacoff, N. Ji, Fast widefield imaging of neuronal structure and function with optical sectioning in vivo. *Sci. Adv.* **6**, eaaz3870 (2020).
8. D. Dan, B. Yao, M. Lei, Structured illumination microscopy for super-resolution and optical sectioning. *Chin. Sci. Bull.* **59**, 1291–1307 (2014).
9. J. L. Killian, F. Ye, M. D. Wang, Optical tweezers: A force to be reckoned with. *Cell* **175**, 1445–1448 (2018).
10. A. Ashkin, J. M. Dziedzic, J. E. Bjorkholm, S. Chu, Observation of a single-beam gradient force optical trap for dielectric particles. *Opt. Lett.* **11**, 288–290 (1986).
11. C. J. Bustamante, Y. R. Chemla, S. Liu, M. D. Wang, Optical tweezers in single-molecule biophysics. *Nat. Rev. Methods Primers* **1**, 25 (2021).
12. X. Li, Y. Yang, S. Yan, W. Gao, Y. Zhou, X. Yu, C. Bai, D. Dan, X. Xu, B. Yao, Artificial potential field-empowered dynamic holographic optical tweezers for particle-array assembly and transformation. *PhotoniX* **5**, 32 (2024).
13. D. G. Grier, A revolution in optical manipulation. *Nature* **424**, 810–816 (2003).
14. X. Li, D. Dan, X. Yu, Y. Zhou, Y. Zhang, W. Gao, M. Li, X. Xu, S. Yan, B. Yao, Concentric ring optical traps for orbital rotation of particles. *Nanophotonics* **12**, 4507–4517 (2023).
15. S. Hohng, R. Zhou, M. K. Nahas, J. Yu, K. Schulten, D. M. J. Lilley, T. Ha, Fluorescence-force spectroscopy maps two-dimensional reaction landscape of the Holliday junction. *Science* **318**, 279–283 (2007).
16. I. Heller, G. Sitters, O. D. Broekmans, G. Farge, C. Menges, W. Wende, S. W. Hell, E. J. G. Peterman, G. J. L. Wuite, STED nanoscopy combined with optical tweezers reveals protein dynamics on densely covered DNA. *Nat. Methods* **10**, 910–916 (2013).
17. R. Diekmann, D. L. Wolfson, C. Spahn, M. Heilemann, M. Schüttpelz, T. Huser, Nanoscopy of bacterial cells immobilized by holographic optical tweezers. *Nat. Commun.* **7**, 13711 (2016).
18. T. Wilson, Optical sectioning in fluorescence microscopy. *J. Microsc.* **242**, 111–116 (2011).
19. L. H. Schaefer, D. Schuster, J. Schaffer, Structured illumination microscopy: Artefact analysis and reduction utilizing a parameter optimization approach. *J. Microsc.* **216**, 165–174 (2004).
20. U. G. Būtaitė, C. Sharp, M. Horodynski, G. M. Gibson, M. J. Padgett, S. Rotter, J. M. Taylor, D. B. Phillips, Photon-efficient optical tweezers via wavefront shaping. *Sci. Adv.* **10**, eadi7792 (2024).
21. X. Xu, M. Nieto-Vesperinas, Y. Zhou, Y. Zhang, M. Li, F. J. Rodríguez-Fortuño, S. Yan, B. Yao, Gradient and curl optical torques. *Nat. Commun.* **15**, 6230 (2024).
22. Y. Hu, J. J. Kingsley-Smith, M. Nikkhou, J. A. Sabin, F. J. Rodríguez-Fortuño, X. Xu, J. Millen, Structured transverse orbital angular momentum probed by a levitated optomechanical sensor. *Nat. Commun.* **14**, 2638 (2023).
23. Y. Mo, K. Wang, L. Li, S. Xing, S. Ye, J. Wen, X. Duan, Z. Luo, W. Gou, T. Chen, Y.-H. Zhang, C. Guo, J. Fan, L. Chen, Quantitative structured illumination microscopy via a physical model-based background filtering algorithm reveals actin dynamics. *Nat. Commun.* **14**, 3089 (2023).
24. J. Schindelin, I. Arganda-Carreras, E. Frise, V. Kaynig, M. Longair, T. Pietzsch, S. Preibisch, C. Rueden, S. Saalfeld, B. Schmid, J.-Y. Tinevez, D. J. White, V. Hartenstein, K. Eliceiri, P. Tomancak, A. Cardona, Fiji: An open-source platform for biological-image analysis. *Nat. Methods* **9**, 676–682 (2012).
25. K. C. Neuman, S. M. Block, Optical trapping. *Rev. Sci. Instrum.* **75**, 2787–2809 (2004).
26. A. Ashkin, J. M. Dziedzic, T. Yamanet, Optical trapping and manipulation of single cells using infrared laser beams. *Nature* **330**, 769–771 (1987).
27. X. Shan, F. Wang, D. Wang, S. Wen, C. Chen, X. Di, P. Nie, J. Liao, Y. Liu, L. Ding, P. J. Reece, D. Jin, Optical tweezers beyond refractive index mismatch using highly doped upconversion nanoparticles. *Nat. Nanotechnol.* **16**, 531–537 (2021).
28. Z. Chen, P. Liu, W. Wang, X. Cao, Y.-X. Liu, Y.-H. Zhang, M. Ge, Rapid sulfate formation via uncatalyzed autoxidation of sulfur dioxide in aerosol microdroplets. *Environ. Sci. Technol.* **56**, 7637–7646 (2022).
29. B. Melo, M. T. Cuairan, G. F. M. Tomassi, N. Meyer, R. Quidant, Vacuum levitation and motion control on chip. *Nat. Nanotechnol.* **19**, 1270–1276 (2024).
30. K. Nakos, M. N. A. Alam, M. R. Radler, I. A. Kesisova, C. Yang, J. Okletey, M. R. Tomasso, S. B. Padrick, T. M. Svitkina, E. T. Spiliotis, Septins mediate a microtubule-actin crosstalk that enables actin growth on microtubules. *Proc. Natl. Acad. Sci. U.S.A.* **119**, e2202803119 (2022).
31. L. Shao, P. Kner, E. H. Rego, M. G. L. Gustafsson, Super-resolution 3D microscopy of live whole cells using structured illumination. *Nat. Methods* **8**, 1044–1046 (2011).
32. D. Li, L. Shao, B.-C. Chen, X. Zhang, M. Zhang, B. Moses, D. E. Milkie, J. R. Beach, J. A. Hammer, M. Pasham, T. Kirchhausen, M. A. Baird, M. W. Davidson, P. Xu, E. Betzig, Extended-resolution structured illumination imaging of endocytic and cytoskeletal dynamics. *Science* **349**, aab3500 (2015).
33. J. Zhou, L. Mei, M. Yu, X. Ma, D. Hou, Z. Yin, X. Liu, Y. Ding, K. Yang, R. Xiao, X. Yuan, Y. Weng, M. Long, T. Hu, J. Hou, Y. Xu, L. Tao, S. Mei, H. Shen, Y. Yalikun, F. Zhou, L. Wang, D. Wang,

S. Liu, C. Lei, Imaging flow cytometry with a real-time throughput beyond 1,000,000 events per second. *Light Sci. Appl.* **14**, 76 (2025).

34. B. Cardenas-Benitez, R. Hurtado, X. Luo, A. P. Lee, Three-dimensional isotropic imaging of live suspension cells enabled by droplet microvortices. *Proc. Natl. Acad. Sci. U.S.A.* **121**, e2408567121 (2024).
35. J. Sun, B. Yang, N. Koukourakis, J. Guck, J. W. Czarske, AI-driven projection tomography with multicore fibre-optic cell rotation. *Nat. Commun.* **15**, 147 (2024).
36. R. Di Leonardo, F. Ianni, G. Ruocco, Computer generation of optimal holograms for optical trap arrays. *Opt. Express* **15**, 1913–1922 (2007).
37. D. Ershov, M.-S. Phan, J. W. Pylvänäinen, S. U. Rigaud, L. Le Blanc, A. Charles-Orszag, J. R. W. Conway, R. F. Laine, N. H. Roy, D. Bonazzi, G. Duménil, G. Jacquemet, J.-Y. Tinevez, TrackMate 7: Integrating state-of-the-art segmentation algorithms into tracking pipelines. *Nat. Methods* **19**, 829–832 (2022).

Acknowledgments

Funding: This work was supported by the National Natural Science Foundation of China under grant nos. 12127805 (B.Y.), 62335018 (B.Y.), 62135005 (S.Y.), and 12274181 (X.X.), the National Key R&D Program of China under grant nos. 2023YFF0613700 (X.X.), 2021YFF0700303 (B.Y.), and 2023YFF1205704 (X.Y.), the Natural Science Basic Research Program of Shaanxi Province under grant no. 2025JC-JCQN-062 (X.X.), and the Innovation Support Program of Shaanxi Province under grant no. 2024ZC-KJXX-069 (X.X.). **Author contributions:** X.X., O.J.F.M., and B.Y. supervised the project. X.L., X.X., and B.Y. conceived the concept of optical tweeze-sectioning microscopy. X.L. was responsible for designing and constructing the experimental setup, as well as acquiring and analyzing the experimental data. D.D., S.Z., Y.Z., and J.Q. provided assistance in experimental data analysis. W.G. and Q.Z. prepared the samples. S.Y. conducted numerical simulations. Y.Y. and X.Y. assisted in figure drawing. X.L. and X.X. wrote the original draft. All authors participated in the review of the manuscript. **Competing interests:** The authors declare that they have no competing interests. **Data and materials availability:** All data needed to evaluate the conclusions in the paper are present in the paper and/or the Supplementary Materials.

Submitted 11 March 2025
Accepted 27 May 2025
Published 2 July 2025
10.1126/sciadv.adx3900